Cancer cells surviving cisplatin chemotherapy increase stress-induced OMA1 activity and mitochondrial fragmentation

Melvin Li[1,2*], Chenille A. McCullum[1], Louis T.A. Rolle[1], Qin Ni[3,4], Zhuoxu Ge[3,4], Sean X. Sun[3,4], Kenneth J. Pienta[1,2], Sarah R. Amend[1,2]

[1]Cancer Ecology Center, The James Brady Urological Institute, Johns Hopkins School of Medicine, Baltimore, MD 21287
[2]Pharmacology and Molecular Sciences Program, Johns Hopkins School of Medicine, Baltimore, MD 21287
[3]Institute for NanoBio Technology, Johns Hopkins University
[4]Department of Mechanical Engineering, Johns Hopkins University
*Correspondence: Melvin Li (mli154@jh.edu)

Author Contact Information
Melvin Li (mli154@jh.edu)
Chenille A. McCullum (cmccul17@jh.edu)
Louis T.A. Rolle (lrolle1@jh.edu)
Qin Ni (qni4@jhu.edu)
Zhuoxu Ge (zge6@jhu.edu)
Sean X. Sun (ssun@jhu.edu)
Kenneth J. Pienta (kpienta1@jhmi.edu)
Sarah R. Amend (samend2@jhmi.edu)

ABSTRACT

Cancer is one of the leading causes of deaths worldwide. Once cancer acquires therapy resistance, it becomes the main driver of cancer lethality in patients. Thus, mechanisms of therapy resistance must be investigated to improve patient outcomes. Mitochondria are critical organelles in the cellular stress responses, undergoing dynamic morphological and functional changes in response to external stimuli. We and others have identified a chemotherapy-resistant cancer cell state where cells that survive treatment exhibit a dramatic increase in cell size and remain non-proliferative for weeks. In this study, we demonstrate that cancer cells that enter this resistant cell state in response to cisplatin increase OMA1 activity and decrease mitochondrial fusion and function to combat oxidative stress. These findings contribute to further understanding the role of the mitochondrial stress responses in therapy resistance in cancer and provide a potential therapeutic avenue to targeting cancer cells that enter this chemotherapy-resistant cell state.

Keywords: cancer, mitochondrial morphology, mitochondrial dynamics, OMA1, OPA1, oxidative stress

INTRODUCTION

Mitochondria are essential organelles that play multi-faceted roles in maintaining cellular homeostasis and stress responses[1,2]. These organelles undergo dynamic morphological changes in response to metabolic and stress stimuli[1,2]. Mitochondrial fission is induced by oxidative stress, resulting in a fragmented phenotype to decrease oxidative capacity or to shuttle damaged mitochondria for degradation via mitophagy[3]. Mitochondrial fusion can be induced by increased energetic demands, creating a hyperfused branching network with increased oxidative capacity[3]. These organelles are dysregulated in many cancers, enabling cells to better obtain resources and adapt to their environment[3]. Recent studies have shown that alterations in mitochondrial morphology and dynamics confer resistance to a wide range of chemotherapies across many tumor types[4-9]. Given the evidence on the role of mitochondria in therapy-resistant cancers, targeting mitochondria is a promising strategy to combat cancer drug resistance.

Our group and others have previously reported that cancer cells that survive chemotherapy enter a resistant cell state in which they increase in size over time and are resistant to subsequent treatments[10-14]. This phenomenon has been reported in mouse models and in human tumors across various tumor types and is induced by multiple classes of chemotherapy and environmental conditions[13-19]. In addition, the presence of this cell state in patient primary tumors predict progression to metastatic disease, further strengthening its significance *in vivo*[13,20,21]. Our previous work has identified that these cells exhibit altered nuclear morphology, a dramatic increase and displacement of intracellular labile iron and lysosomes, and increased antioxidant responses through NRF2 signaling[10,22]. Mitochondria interact with all these processes, including communicating with the nucleus through retrograde signaling, storing labile iron in iron-sulfur clusters, colocalizing with lysosomes to degrade damaged portions of mitochondria, and undergoing turnover in response to NRF2 signaling[23-28].

Mitochondrial mass has been reported to increase in cancer cells entering this resistant state from paclitaxel treatment in breast cancer, while another study observed increased mitophagy in cancer cells surviving chemotherapy treatment in a head and neck cancer model[29,30]. Beyond these observations, the molecular mechanisms of the mitochondrial phenotypes in this chemotherapy-resistant cancer cell state have been largely unexplored. In this study, we investigated mitochondrial morphology, dynamics, and stress responses in prostate cancer cells surviving cisplatin chemotherapy. Through various imaging modalities and

protein expression analyses, we identified that the cells surviving chemotherapy exhibit increased OMA1 activity, aberrant cristae morphology, and reduced mitochondrial fusion, leading to decreased mitochondrial function. Our findings suggest that targeting OMA1 activity could be a potential therapeutic vulnerability specific to this resistant phenotype.

RESULTS

Cancer cells surviving chemotherapy exhibit increased levels of reactive oxygen species and increased mitochondrial fragmentation. The PC3 prostate cancer cell line was treated with an LD50 dose of cisplatin (6 μM) for 72 hours[10,31]. At the end of treatment, cisplatin-containing media was removed, and the surviving cells were then cultured in fresh media for up to 10 days (**Fig. 1A**). During the 10-day period after cisplatin removal, surviving cells were not proliferative and increased in cell size over time, resulting in a 40-fold increase in cell volume at 10 Days Post-Treatment Removal (10 Days PTR) (**Fig. 1B-C**). We have previously published that cells continue to die after treatment removal, and the death rate plateaus at 10 Days PTR[10]. We initially hypothesized that these surviving cells have recovered from the cellular damage induced by chemotherapy, including the increased oxidative stress and DNA damage induced by chemotherapy treatment[32]. We found that the cells 10 Days PTR exhibited increased levels of reactive oxygen species (ROS) per cell area when compared to untreated cells (**Fig. 1D-E**). To validate this finding, both groups were treated with antioxidant N-acetyl cystine (NAC) for 24 hours. While the PC3 cells did not show any change in DCF-DA staining, cells 10 Days PTR exhibited a decrease in DCF-DA staining under NAC-treated conditions, (**Supplementary Fig. S1**).

Mitochondrial morphology is altered under oxidative stress[33]. We observed that cells 10 Days PTR have more mitochondria on a per cell basis, although this difference is non-significant when normalizing to cell area (**Fig. 1F-H**). Quantification of mitochondrial morphology showed that cells 10 Days PTR exhibited mitochondrial fragmentation, with a 1.5-fold decrease in branches per mitochondrion and a 1.5-fold decrease in branch length per mitochondrion (**Fig. 1F, I-J**).

Surviving cells increase DRP1 localization to mitochondria. Mitochondrial fragmentation can be the result of an increase in fission or a decrease in fusion[34]. We probed for the expression of dynamin-related GTPases that are known to remodel mitochondrial structure. Dynamin-related protein 1 (DRP1) is the main driver of mitochondrial fission at the outer mitochondrial membrane (OMM) upon translocation from the cytosol to the mitochondria. Phosphorylation of DRP1 at Ser616 promotes its translocation to the OMM, while phosphorylation of DRP1 at Ser637 prevents the translocation from occurring[1]. Total DRP1 expression was unchanged in cells 10 days PTR compared to control and Ser616 phosphorylation was not detected in either group (**Fig. 2A**). Cells 10 Days PTR had decreased DRP1 Ser637 phosphorylation compared to untreated cells, suggesting a decrease in DRP1 inhibition and an increase in DRP1 localization to mitochondria (**Fig. 2A**). DRP1 binds to receptors mitochondrial fission factor (MFF), MiD49, or MiD51 on the OMM that allow DRP1 to assemble on the mitochondrial surface for its fission activity[1,2,35]. Compared to control, cells 10 Days PTR showed increased expression of MFF and MiD49, but a decrease in MiD51 expression (**Fig. 2A**). We next assessed DRP1 mitochondrial localization via immunofluorescence. Cells 10 Days PTR had increased DRP1-mitochondria localization when compared to PC3 control cells (**Fig. 2B-F**). These results suggest that DRP1 may play a role in the fragmentation phenotype that we observe in the mitochondria of surviving cells.

Mitochondria in surviving cells exhibit aberrant cristae morphology. In addition to DRP1-mediated fission, mitochondrial fragmentation can occur through a decrease in fusion, which is

153 mainly regulated by Mitofusin 1 (MFN1), Mitofusin 2 (MFN2), and optic atrophy 1 protein (OPA1)
154 [1,35]. MFN1 and MFN2 are responsible for the fusion of the OMM [1]. There were no differences in
155 MFN1 and MFN2 expression between surviving cells and untreated cells (**Fig. 3A**). OPA1 is an
156 inner membrane remodeler that maintains cristae structure[1,35]. The long isoforms of OPA1
157 mediate fusion of the inner mitochondrial membrane and promote tight stacking of lamellar
158 cristae[36,37]. Under oxidative stress or mitochondrial depolarization, OPA1 is cleaved by OMA1
159 into short isoforms (L1 to S3, and L2 to S5), leading to decreases in mitochondrial fusion and
160 energetic capacity[37-39].
161 Cells that survived cisplatin treatment showed a decrease in the L2 isoform of OPA1 and
162 an increase of the S5 isoform, suggesting that L-OPA1 is cleaved to S-OPA1 by OMA1 (**Fig.**
163 **3A-B**). Upon stress conditions, OMA1 cleaves itself when activated to act on L-OPA1[39,40]. We
164 observed decreased expression of OMA1 in cells 10 Days PTR when compared to PC3 control
165 (**Fig. 3A, C**). Taken together, the altered levels of L2 and S5 isoforms of OPA1 and decreased
166 OMA1 levels in cells 10 Days PTR suggest OMA1 activity is higher in the cells that survive
167 cisplatin than control.
168 OPA1 is responsible for maintaining mitochondrial cristae structure. To evaluate this
169 directly, we performed transmission electron microscopy (TEM) to assess mitochondrial cristae
170 morphology. Mitochondria in untreated cells had tight lamellar cristae, while the mitochondria in
171 cells 10 Days PTR exhibited amorphous and wider cristae shape (**Fig. 3D**). Quantification of
172 cristae morphology showed that mitochondria in cells 10 Days PTR had fewer cristae, higher
173 mean cristae area, and higher cristae width (**Fig. 3E-G**). In addition, mitochondria in in cells 10
174 Days PTR were 3.5 times smaller by area than the mitochondria in untreated cells, supporting
175 the fragmentation phenotype that we observed in the immunofluorescence imaging in **Figure**
176 **1F, I-J** (**Fig. 3H**).
177 Overall, these data indicate that mitochondria in cells 10 Days PTR have impaired
178 cristae organization. The complexes of the electron transport chain (ETC) reside on the cristae
179 structure. The ETC complexes generate a negative membrane potential ($\Delta\Psi_m$) across the inner
180 mitochondrial membrane (IMM) as electrons are shuttled through[41]. To assess the functional
181 implications of this altered mitochondrial cristae structure, we measured the mitochondrial
182 membrane potential via live-cell staining with MitoTracker Red CMXRos. We observed that the
183 mitochondria in cells 10 Days PTR had decreased MitoTracker Red CMXRos signal when
184 compared to untreated cells, indicating that mitochondria are less active in cells 10 Days PTR
185 (**Fig. 3I-J**).
186
187 **Cells that survive cisplatin treatment decrease both mitochondrial fission and fusion**
188 **dynamics**. Given the changes in both DRP1 phosphorylation and OPA1 processing in cells 10
189 Days PTR, we next directly evaluated mitochondrial fission and fusion dynamics. We performed
190 time lapse imaging to capture mitochondrial fission and fusion events on a per-mitochondrion
191 basis, taking an image every 30 seconds for a total of 15 minutes. Overall, we observed that the
192 fission and fusion rate scaled with increasing mitochondrial area (**Fig. 4A-C**). When normalized
193 to mitochondrial area, cells 10 Days PTR had a 50% decrease in fission rate and a 50%
194 decrease in fusion rate than untreated cells (**Fig. 4A, D-E, Supplementary Video 1-4**).
195
196 **DISCUSSION**
197
198 Given the critical roles of mitochondria in cellular stress responses and their implications
199 in therapy-resistant cancer cells, recent advancements in identifying molecular regulators that
200 drive morphological and functional adaptations provide potential therapeutic avenues for
201 cancer[3,4,6,35,42]. Our group and others have reported the emergence of an enlarged and non-
202 proliferative cancer cell state in response to various chemotherapy treatments [10-14,22]. These
203 cells are resistant to subsequent chemotherapy and are associated with worse prognosis in

mouse models and in patients[13-20]. In this study, we evaluated the mitochondrial stress responses in cancer cells that survive in the days following chemotherapy.

These cells 10 Days PTR had increased levels of ROS (**Fig. 1D-E**), consistent with previous reports in bladder cancer where giant cells that emerge after cisplatin treatment survive with increased levels of ROS[43]. The accumulation of ROS can induce oxidation of macromolecules that are essential for cellular homeostasis, leading to DNA damage, misfolding of proteins, and lipid peroxidation[44-47]. We have previously published that cells surviving chemotherapy have continued DNA damage response (DDR), even at 10- and 15-Days PTR[10]. and that cells 10 Days PTR exhibit increased lipid peroxidation[22]. Moreover, this work also showed that these surviving cells have an increase in nuclear factor erythroid 2-related factor (NRF2)-mediated antioxidant response, further demonstrating that they are in a state of oxidative stress[22].

Mitochondrial biogenesis, morphology, and function are altered under oxidative stress[33,48-51]. While we observe that surviving cells have more mitochondria on a per cell basis, when normalizing to cell size, there was no difference in mitochondrial number (**Fig. 1F-H**). When analyzing the structure of the mitochondria, we found that the mitochondria in cells 10 Days PTR were more fragmented and had fewer branches per mitochondrion when compared to the mitochondria of the untreated cells (**Fig. 1F, I-J**). We hypothesize that mitochondria in surviving cells underwent fragmentation in response to the increase in ROS levels when compared to untreated cells. Building on observations of this fragmentation phenotype in other in cancer cells subjected to oxidative stress[48,50,52], our findings align with recent work by Song et al. showing that cancer cells with a similar morphological phenotype that survive paclitaxel treatment had more mitochondria per cell but exhibited a smaller and more fragmented phenotype when compared to the untreated controls[53]. The mitochondria in those surviving cells also moved more slowly and had fewer fission and fusion events than the mitochondria in the control cells[53]. This suggests that these treatment-induced mitochondrial phenotypes could span across therapies that act through different mechanisms, as paclitaxel is a microtubule stabilizer, while cisplatin creates adducts in purine bases and ultimately causes DNA double strand breaks[54,55].

When probing for the expression of the molecular regulators of mitochondrial fusion, we identified differential expression of multiple isoforms of OPA1 when comparing cells 10 Days PTR and untreated cells (**Fig. 3A-B**). The decrease in L2-OPA1 and increase in S5-OPA1 expression suggested that the stress-induced protease OMA1 was active in cells 10 Days PTR (**Fig. 3A-B**). This is further supported by the decreased level of OMA1 itself, likely due to its autocatalytic turnover. The S3 and S5 isoforms of OPA1 are fusion incompetent, and have been shown to induce mitochondrial fission through interactions with DRP1 and other fission machinery and were shown to be protective in events of oxidative stress[38,56]. The accumulation of these OPA1 isoforms may be a mechanism to reduce mitochondrial fusion and decrease OXPHOS to prevent further production of ROS, as mitochondria are major sources of intracellular ROS when electrons are shuttled through the ETC[49].

We observed that the mitochondria in cells 10 Days PTR had larger and more amorphous cristae than the tight, lamellar cristae in the mitochondria of untreated cells (**Fig. 3D-H**). This aberrant morphology can be attributed to the decrease in L-OPA1 and accumulation of S-OPA1 via OMA1 cleavage (**Fig. 3A-C**), as the short isoforms are not tethered to the IMM to promote cristae folding[36,39,40]. Cristae folding increases the surface area of the IMM for oxidative phosphorylation by bringing electron transport chain (ETC) complexes closer together and concentrating the proton gradient[36,57,58]. Cells 10 Days PTR had decreased ETC efficiency of (**Fig. 3I-J**). It has been reported that cells engineered to express S-OPA1 exclusively have higher survival under oxidative stress than cells engineered to express only L-OPA1[56]. Cells expressing solely L-OPA1 produced more superoxide radicals and therefore were sensitized to oxidative stress[56]. Thus, the decrease in cristae folding in surviving cells further supports that

surviving cells may reduce OXPHOS and subsequent endogenous ROS production in response to oxidative stress.

Mitochondrial morphology is mediated by dynamic fission and fusion processes. We observed a surprising decrease in the mitochondrial fission rate in cells 10 Days PTR (**Fig. 4A, D**). This was unexpected given the parallel findings of increased DRP1 localization to mitochondria (via TOM20-DRP1 colocalization analysis), increased expression of MFF and MiD49, and decreased expression of phospho-DRP1 Ser637 (**Fig. 2A-F**). This may suggest an increase in the upstream signaling to promote mitochondrial fission, but a mechanism downstream of DRP1 leading to the decreased fission rate we observed in the time lapse imaging. There are several factors that affect mitochondrial fission after DRP1 docks onto the various receptors on the OMM. The endoplasmic reticulum (ER) is a significant player in mitochondrial fission. The molecular regulators of mitochondrial fission and fusion colocalize with ER-mitochondrial contact sites to regulate mitochondrial dynamics[59,60]. The polymerization of actin around the ER and the mitochondria and the transfer of calcium from the ER to mitochondria mediate the constriction of the outer mitochondrial membrane that is required for mitochondrial fission to occur[61-64]. Cells 10 Days PTR may have decreased ER-mitochondrial contacts, which could explain the paradoxical increase in DRP1 localization to mitochondria and a decrease in mitochondrial fission rate, but this has yet to be tested. Based on the TEM images in **Figure 3D**, the ER appear more fragmented and further from mitochondria in cells 10 Days PTR when compared to the ER in the PC3 control cells. Cytoskeletal filaments also play important roles in regulating mitochondrial fission, although their effects may be cell type or context specific. In a model of *X. laevis* melanocytes, depolymerizing microtubules with nocodazole decreased mitochondrial distribution, motility, and shape dynamics across the entire cell[65], while mitochondrial associations with microtubules inhibited mitochondrial fission in a model of fission yeast[66]. How the cytoskeleton filaments affect mitochondrial dynamics in cancer cells in this resistant state is unknown and warrants further investigation. In addition to decreased mitochondrial fission rate, cells 10 Days PTR also exhibited a decrease in the rate of mitochondrial fusion (**Fig. 4A, E**). This data coincides with the increased OMA1 activity, decreased expression of the fusion-promoting L-OPA1 isoforms, and increased expression of the fusion-incompetent S-OPA1 isoforms we observed from **Fig. 3A-C**. The decrease in mitochondrial fusion could also lead to the fragmentation phenotype we observed in the mitochondria of the cells 10 Days PTR (**Fig. 1F, I-J**).

In summary, our findings suggest that cancer cells surviving chemotherapy increase OMA1 activity in response to oxidative stress. The stress-induced OMA1 activity cleaves OPA1 into its shorter isoforms, leading to a decrease in mitochondrial fusion, aberrant mitochondrial cristae morphology, and decreased efficiency of oxidative phosphorylation, ultimately promoting cell survival under increased ROS conditions (**Fig. 5**). Although there are currently no specific OMA1 inhibitors developed, this work contributes to the need for the screening of compounds against OMA1 activity, as other groups have solely used genetic mechanisms to inhibit OMA1 in various cancer models[42,67-69]. Further work involves knocking out OMA1 in PC3 cells to assess its role in the entrance to this cancer cell state. We hypothesize that these surviving cancer cells are critical mediator of cancer lethality in patients. Additional characterization of the cellular stress responses and molecular programs of cells in this resistant state will shine light on potential vulnerabilities that can be leveraged to target them for destruction and improve patient prognosis.

MATERIALS AND METHODS

Cell culture. The PC3 cell line was purchased from American Type Culture Collection (ATCC). Cells were cultured in RPMI 1640 medium (ThermoScientific; Cat# 11875119) with 10% fetal

305 bovine serum (FBS) (Avantar; Cat# 97068-085) and 1% penicillin and streptomycin (P/S)
306 (Gibco; Cat#15140-122). Cells were incubated at 37℃ and 5% CO2.
307
308 ***Induction of resistant cancer cell state.*** PC3 cells were plated in 150 mm dishes (Corning;
309 Cat#: 353025) at a density of 1,250,000 cells per dish. 24 hours after seeding, cells were
310 treated with an IC50 dose (6μM) of cisplatin (Millipore Sigma; Cat#: 232120) in RPMI media with
311 10% FBS and 1% P/S for 72 hours. Drug-containing media was then removed, and fresh cell
312 culture media was added onto surviving cells. The surviving cells were monitored for 10 days,
313 with media changes every 3 days. Cells were analyzed 10-days post-treatment removal (PTR)
314 for all experiments.
315
316 ***Phase contrast microscopy.*** Cells were cultured to their desired timepoint in T75 flasks.
317 Phase contrast microscopy was performed on an EVOS M7000 (ThermoScientific) with a 10X
318 objective.
319
320 **Cell volume measurement with Fluorescence eXclusion method**. The microfluidic
321 Fluorescence Exclusion method (FXm) was used to measure the volume of PC3 untreated cells
322 and cells 10 Days PTR [101, 102]. In this method, microfluidic channels with known heights
323 were fabricated. Cells were seeded into the device in the presence of a membrane-
324 impermeable fluorescent dextran and imaged using an epifluorescence microscope. The
325 reduction in fluorescence intensity due to cell volume exclusion is proportional to the ratio
326 between the cell height and the channel height, allowing us to calculate cell volume. FXm
327 channel fabrication and volume calculation are described in previously published work by Ni et
328 al. and Rochman et al. [102, 103].
329
330 ***Immunofluorescence and Airyscan super-resolution imaging.*** Cells were plated onto poly-l-
331 lysine coated coverslips (Thomas Scientific; Cat#: 1217N79). Cells were fixed with methanol-
332 free 4% paraformaldehyde (ThermoFisher Scientific; Cat#28908) in 1X PBS for 15 minutes at
333 room temperature followed by permeabilization with 0.2% Triton-X 100 (ThermoFisher
334 Scientific; Cat#28314) in 1X PBS for 10 minutes at room temperature. Blocking was performed
335 with 10% Normal Goat Serum (abcam; Cat# ab7481) in 0.1% PBS-Tween20 for 30 minutes at
336 room temperature. Cells were incubated with primary antibody diluted in 10% Normal Goat
337 Serum in 0.1% PBS-Tween20 overnight at 4℃: anti-Tom20 (Santa Cruz; Cat# sc-17764) diluted
338 1:100 and anti-DRP1 (Cell Signaling Technology; Cat#: 8570S) diluted 1:100. Secondary
339 antibody incubation was performed using Goat anti-mouse IgG2a Cross-Absorbed Alexa Fluor
340 647 (ThermoFisher Scientific; Cat# A-21131) and Goat anti-rabbit IgG (H+L) Highly Cross-
341 Absorbed Secondary Alexa Fluor Plus 555 diluted 1:1000 in 10% Normal Goat Serum in 0.1%
342 PBS-Tween20 for 1 hour. Cells were also stained for F-actin during the secondary antibody
343 incubation with Alexa Fluor 488 Phalloidin (ThermoFisher Scientific; Cat# A22287). Following
344 secondary antibody and phalloidin incubation, cells were washed with 0.1% PBS-Tween20
345 three times and subsequently washed twice with 1X PBS. Coverslips were washed once in
346 dH2O prior to mounting. Coverslips were mounted onto slides with 10 μL of Prolong Glass
347 Antifade Mountant (ThermoFisher Scientific; Cat#: P36984) and samples were cured for at least
348 50 hours prior to imaging. All slides were imaged on a Zeiss LSM 880 microscope (Carl Zeiss)
349 in Airyscan SR mode with an 63X, numerical aperture 1.4 PlanApo oil objective. Images were
350 taken in a 3X3 tile z-stack at a resolution of 1768X1768 pixels per tile and an axial step size of
351 187 nm. 3D Airyscan Joint Deconvolution was performed on Zen software for image processing
352 and downstream image analyses were performed in ImageJ[70] and Imaris (Bitplane).
353
354 ***Mitochondrial morphology analysis.*** Images were imported into ImageJ[70] and converted to 8-
355 bit images. The ImageJ pipeline, Mitochondria Analyzer, was used to analyze mitochondrial

356 morphology[71]. In short, 3D thresholding was performed on each image within the Mitochondria
357 Analyzer plugin[71]. The settings used were Rolling = 1.0, Max Radius = 1.25, Block Size = 3, C-
358 Value = 3-5, Post-Processing Outlier Radius = 8.0 – 9.823 pixels. 2D slices were then obtained
359 from the 3D thresholded images for 2D mitochondrial morphology analysis. Features such as
360 branches per mitochondrion and branch length per mitochondrion were extracted in the
361 Mitochondria Analyzer plugin with the 2D thresholded slices as input images.
362
363 ***Colocalization analysis.*** In 2D, images were imported into ImageJ[70] and split into individual
364 channels and maximum Z-projections were generated for each channel. A line drawing was
365 used to generate intensity profiles along the length of the line. Intensities were normalized within
366 the DRP1 and Tom20 channel and overlayed together into a graph using RStudio[72] with
367 ggplot2[73]. For 3D analysis, images were analyzed in Imaris (Bitplane) for Tom20-DRP1
368 colocalization. Background subtraction was applied using a 10 µm filter, then surface renderings
369 were generated of the Tom20 and DRP1 channels. Using the object-to-object statistics
370 parameter, only DRP1 that was touching the Tom20 surface (0.0 µm away) was filtered for, and
371 a separate surface channel was created to only include those DRP1 surfaces. Percent
372 colocalization per cell was determined by taking the number of colocalized DRP1 surfaces
373 divided by the total number of DRP1 surfaces in the cell, multiplied by 100.
374
375 ***Mitochondrial membrane potential imaging and analysis.*** Cells were plated into a black 24-
376 well plate (ibidi; Cat# 82426) and allowed to adhere overnight. Cells were stained with 100 nM
377 MitoTracker Red CMXRos (ThermoScientific; Cat#: M7512) for 30 minutes at 37℃ and 5% CO2
378 and washed twice with 1X PBS. RPMI phenol red-free media containing 10% FBS and 1% P/S
379 was then added into each well of the 24-well plate and cells were imaged on an EVOS M7000
380 high content imager (ThermoScientific) with 37℃ and 5% CO2 incubation. Images were
381 analyzed in CellProfiler[74] for mean fluorescence intensity of MitoTracker Red CMXRos staining.
382
383 ***Transmission electron microscopy and mitochondrial cristae morphology analysis.***
384 Transmission electron microscopy sample prep was performed with a previously published
385 protocol from Kostecka et al.[75]. Briefly, cells were cultured to the desired timepoints and were
386 fixed overnight at 4℃ in a solution of 2.5% glutaraldehyde, 3mM MgCl2, in 0.1 M sodium
387 cacodylate buffer, pH 7.2. Samples were rinsed with buffer followed by additional fixation in the
388 dark and on ice for 1 hour with 1% osmium tetroxide reduced with 1.5% potassium ferrocyanide
389 in 0.1 M sodium cacodylate buffer. Samples were rinsed with dH2O rinse and en bloc staining
390 was performed for one hour in 2% uranyl acetate (aq). A graded series of ethanol was used to
391 dehydrate the samples and samples were then embedded in Eponate resin overnight at 60℃. A
392 diamond knife on the Reichert-Jung Ultracut E ultramicrotome was used to cut 60 to 90 nm
393 sections. 2x1 mm formvar coated copper slot grids were used to pick up the sections. 2% uranyl
394 acetate (aq.) and 0.4% lead citrate were used to stain the grids before imaging on a
395 ThermoFisher Talos L120C at 120 kV with a ThermoFisher Ceta CCD (16 megapixel CMOS,
396 16-bit).
397
398 ***Time lapse microscopy for mitochondrial dynamics***. Cells were plated into 8-well ibiTreat µ-
399 slides (ibidi; Cat#: 80826) and allowed to adhere overnight. Cells were stained with 150 nM
400 MitoTracker Green (ThermoScientific; Cat#: M7514) for 30 minutes at 37℃ and 5% CO2 and
401 washed twice with 1X PBS. RPMI phenol red-free media containing 10% FBS and 1% P/S was
402 then added into each well of the 8-well ibiTreat µ-slide. Cells were imaged on a Zeiss LSM 880
403 microscope (Carl Zeiss) in Airyscan SR mode with an 63X, numerical aperture 1.4 PlanApo oil
404 objective, at 37℃ and humidified 5% CO2. Cells were excited with a 488 nm laser and 2D
405 images were taken every 30 seconds for 15 minutes at a resolution of 1280X1280 pixels to
406 observe mitochondrial fission and fusion events. 2D Airyscan Processing was performed in Zen

software, and images were then subjected to background subtraction in ImageJ[70] using the rolling ball method with a radius of 50 pixels. Mitochondrial fission and fusion events were identified through Mitometer, a MATLAB-based software to track mitochondria over time[76].

Western blot. PC3 control cells and cells 10 Days PTR were lifted from T150 flasks with TrypLETM Express (GibcoTM; Ref# 12604-013) in lysate form using a RIPA buffer (Sigma-Aldrich; Cat#: R0278-500ML) with Halt Protease & Phosphatase cocktail (ThermoScientific; Cat#: 78440) and 0.5M EDTA (ThermoScientific; Cat#: 1861274). Lysates were incubated at 4℃ on a rotator for 30 minutes and then were subsequently spun in a 4℃ centrifuge at 21,000 rcf and stored at -20℃. The Pierce BCA Protein Assay was used to equally allocate 50 µg protein from each lysate for each lane being run in the gel. Each sample was made with the appropriate amount of lysate, 5 µL 4X Loading Buffer (4X Laemmli Buffer (Bio-Rad #1610747), beta-Mercaptoethanol (Bio-Rad; Cat#: 1610710XTU), and completed with UltraPure distilled water (ThermoScientific; Cat#: 10977023). Samples were boiled in a thermocycler set to 99℃ with a lid temperature of 105℃ for 10 minutes. A 4-20% Mini-PROTEAN TGX gel (Bio-Rad #4561094) was loaded with each sample and Chameleon Duo Pre-stained Protein Ladder (LI-COR Biosciences; Cat#: 928-60000). The gel run was set at 140 V for 60 minutes. For OPA1 probing, a 7.5% Mini-PROTEAN TGX gel (Bio-Rad #4561023) was used, and gels were run at 50 V for 300 minutes. Gels were transferred onto a 0.2 µm nitrocellulose membrane in the Trans-Blot Turbo Transfer Pack (Bio-Rad; Cat#: 1704158) using the BioRad Trans-Blot Turbo Transfer System. The membrane was blocked in 1X Casein Buffer (10X Casein Buffer (Sigma-Aldrich; Cat#: B6429-500ML) diluted with UltraPure distilled water on a room temperature shaker for 1 hour. The membrane was then incubated in a primary antibody specific to the target protein at a 1:1000 dilution in 1X Casein Buffer with mouse β-actin primary antibody (Sigma Aldrich; Cat#: A5441-0.5ML) at 1:5000 dilution overnight at 4℃. The primary antibodies used were Phospho-DRP1 Ser616 (Cell Signaling Technology; Cat# 3455S), Phospho-DRP1 Ser637 (Cell Signaling Technology; Cat#: 4867S), DRP1 (Cell Signaling Technology; Cat#: 8570S), MFF (Cell Signaling Technology; Cat#: 84580S), MiD49 (Proteintech; Cat# 28718-1-AP), MiD51 (Proteintech; Cat#: 20164-1-AP), OPA1 (Cell Signaling Technology; Cat#: 80471S), OMA1 (Cell Signaling Technology; Cat#: 95473S), MFN1 (Cell Signaling Technology; Cat#: 14739S), MFN2 (Cell Signaling Technology; Cat#: 9482S). For the OPA1 blots, Vinculin was used as the loading control (Cell Signaling; Cat#: 13901S) at a 1:1000 dilution. The following day, the membrane was washed four times for 5 minutes each in 0.1% TBS-Tween 20 (UltraPure distilled water, 10X TBS (Quality Biological #351-086-101CS), 0.1% Tween 20 (Sigma-Aldrich #9005645)). Then, the membrane was incubated in a secondary antibody diluted in 1X Casein Buffer for 1 hour on a room temperature shaker. The secondary antibodies used were IRdye® 800CW goat anti-rabbit IgG at a 1:15000 dilution, and IRdye® 680RD goat anti-mouse IgG at a 1:20000 dilution (LI-COR Biosciences; Cat# 926-32211 and 926-68070, respectively). The membrane was washed another four times for 5 minutes each in 0.1% TBS-Tween 20. Imaging was performed on the Azure Sapphire. (Azure Biosystems).

Statistics. Statistical analyses were performed in GraphPad Prism version 9.1 (GraphPad Software, LLC) and RStudio[72]. Statistical tests performed are reported in respective figure legends. An alpha value of 0.05 was used for all tests. ns, *, **, ***, and **** indicated $p>0.05$, $p<0.05$, $p<0.01$, $p<0.001$, and $p<0.0001$, respectively. In the violin plots, the solid line represents the median and the dotted lines represent the lower and upper quartiles.

DATA AVAILABILITY

Data is provided within the manuscript or in supplementary information files.

REFERENCES

1 Giacomello, M., Pyakurel, A., Glytsou, C. & Scorrano, L. A.-O. The cell biology of mitochondrial membrane dynamics.

2 Wai, T. Is mitochondrial morphology important for cellular physiology? LID - S1043-2760(24)00123-1 [pii] LID - 10.1016/j.tem.2024.05.005 [doi].

3 Jin, P. *et al.* Mitochondrial adaptation in cancer drug resistance: prevalence, mechanisms, and management. *Journal of Hematology & Oncology* **15**, 97 (2022). https://doi.org:10.1186/s13045-022-01313-4

4 Huang, Q. *et al.* Increased mitochondrial fission promotes autophagy and hepatocellular carcinoma cell survival through the ROS-modulated coordinated regulation of the NFKB and TP53 pathways.

5 Tomková, V., Sandoval-Acuña, C., Torrealba, N. & Truksa, J. Mitochondrial fragmentation, elevated mitochondrial superoxide and respiratory supercomplexes disassembly is connected with the tamoxifen-resistant phenotype of breast cancer cells. *Free Radical Biology and Medicine* **143**, 510-521 (2019). https://doi.org:https://doi.org/10.1016/j.freeradbiomed.2019.09.004

6 Decker, C. W. *et al.* Mitofusin-2 mediates doxorubicin sensitivity and acute resistance in Jurkat leukemia cells.

7 Li, S. A.-O., Wu, Y., Ding, Y., Yu, M. & Ai, Z. CerS6 regulates cisplatin resistance in oral squamous cell carcinoma by altering mitochondrial fission and autophagy.

8 Han, Y. *et al.* Mitochondrial fission causes cisplatin resistance under hypoxic conditions via ROS in ovarian cancer cells. *Oncogene* **38**, 7089-7105 (2019). https://doi.org:10.1038/s41388-019-0949-5

9 Chen, X. *et al.* Targeting Mitochondrial Structure Sensitizes Acute Myeloid Leukemia to Venetoclax Treatment. *Cancer Discovery* **9**, 890-909 (2019). https://doi.org:10.1158/2159-8290.CD-19-0117

10 Kim, C. J. *et al.* Nuclear morphology predicts cell survival to cisplatin chemotherapy.

11 Niu, N. *et al.* Linking genomic reorganization to tumor initiation via the giant cell cycle. *Oncogenesis* **5**, e281-e281 (2016). https://doi.org:10.1038/oncsis.2016.75

12 Pienta, K. A.-O., Hammarlund, E. U., Brown, J. S., Amend, S. A.-O. & Axelrod, R. A.-O. Cancer recurrence and lethality are enabled by enhanced survival and reversible cell cycle arrest of polyaneuploid cells. LID - 10.1073/pnas.2020838118 [doi] LID - e2020838118.

13 Fei, F. *et al.* The number of polyploid giant cancer cells and epithelial-mesenchymal transition-related proteins are associated with invasion and metastasis in human breast cancer. *Journal of Experimental & Clinical Cancer Research* **34**, 158 (2015). https://doi.org:10.1186/s13046-015-0277-8

14 Schmidt, M. J. *et al.* Polyploid cancer cells reveal signatures of chemotherapy resistance. *Oncogene* **44**, 439-449 (2025). https://doi.org:10.1038/s41388-024-03212-z

15 Zhang, X. *et al.* Targeting polyploid giant cancer cells potentiates a therapeutic response and overcomes resistance to PARP inhibitors in ovarian cancer. *Science Advances* **9**, eadf7195 https://doi.org:10.1126/sciadv.adf7195

16 Zhang, S. *et al.* Generation of cancer stem-like cells through the formation of polyploid giant cancer cells. *Oncogene* **33**, 116-128 (2014). https://doi.org:10.1038/onc.2013.96

502 17 Mannan, R. *et al.* Polypoidal giant cancer cells in metastatic castration-resistant prostate
503 cancer: observations from the Michigan Legacy Tissue Program. *Medical Oncology* **37**,
504 16 (2020). https://doi.org:10.1007/s12032-020-1341-6
505 18 Amend, S. A.-O. *et al.* Polyploid giant cancer cells: Unrecognized actuators of
506 tumorigenesis, metastasis, and resistance.
507 19 Lopez-Sánchez, L. M. *et al.* CoCl2, a mimic of hypoxia, induces formation of polyploid
508 giant cells with stem characteristics in colon cancer.
509 20 Trabzonlu, L., Pienta, K. J., Trock, B. J., De Marzo, A. A.-O. & Amend, S. A.-O. Presence of
510 cells in the polyaneuploid cancer cell (PACC) state predicts the risk of recurrence in
511 prostate cancer.
512 21 Alharbi, A. M., De Marzo Am Fau - Hicks, J. L., Hicks Jl Fau - Lotan, T. L., Lotan Tl Fau -
513 Epstein, J. I. & Epstein, J. I. Prostatic Adenocarcinoma With Focal Pleomorphic Giant Cell
514 Features: A Series of 30 Cases.
515 22 Loftus, L. V., Rolle, L. T. A., Wang, B., Pienta, K. J. & Amend, S. R. Dysregulation of Labile
516 Iron Predisposes Chemotherapy Resistant Cancer Cells to Ferroptosis. *International*
517 *Journal of Molecular Sciences* **26** (2025).
518 23 Yang, D. & Kim, J. A.-O. Mitochondrial Retrograde Signalling and Metabolic Alterations in
519 the Tumour Microenvironment. LID - 10.3390/cells8030275 [doi] LID - 275.
520 24 Braymer, J. J. & Lill, R. Iron-sulfur cluster biogenesis and trafficking in mitochondria.
521 25 Wong, Y. C., Ysselstein, D. & Krainc, D. Mitochondria–lysosome contacts regulate
522 mitochondrial fission via RAB7 GTP hydrolysis. *Nature* **554**, 382-386 (2018).
523 https://doi.org:10.1038/nature25486
524 26 Chen, Q. *et al.* Nanoscale monitoring of mitochondria and lysosome interactions for
525 drug screening and discovery. *Nano Research* **12**, 1009-1015 (2019).
526 https://doi.org:10.1007/s12274-019-2331-x
527 27 Wong, Y. C., Kim, S., Peng, W. & Krainc, D. Regulation and Function of Mitochondria–
528 Lysosome Membrane Contact Sites in Cellular Homeostasis. *Trends in Cell Biology* **29**,
529 500-513 (2019). https://doi.org:https://doi.org/10.1016/j.tcb.2019.02.004
530 28 Luchkova, A., Mata, A. & Cadenas, S. A.-O. Nrf2 as a regulator of energy metabolism and
531 mitochondrial function.
532 29 Sirois, I. *et al.* A Unique Morphological Phenotype in Chemoresistant Triple-Negative
533 Breast Cancer Reveals Metabolic Reprogramming and PLIN4 Expression as a Molecular
534 Vulnerability.
535 30 You, B. *et al.* AMPK-mTOR-Mediated Activation of Autophagy Promotes Formation of
536 Dormant Polyploid Giant Cancer Cells.
537 31 Mallin, M. M. *et al.* Cells in the polyaneuploid cancer cell (PACC) state have increased
538 metastatic potential.
539 32 Yang, H. *et al.* The role of cellular reactive oxygen species in cancer chemotherapy.
540 33 Xu, X., Pang, Y. & Fan, X. Mitochondria in oxidative stress, inflammation and aging: from
541 mechanisms to therapeutic advances. *Signal Transduction and Targeted Therapy* **10**, 190
542 (2025). https://doi.org:10.1038/s41392-025-02253-4
543 34 Berman, S. B., Pineda Fj Fau - Hardwick, J. M. & Hardwick, J. M. Mitochondrial fission
544 and fusion dynamics: the long and short of it.

35 Tilokani, L., Nagashima, S., Paupe, V. & Prudent, J. Mitochondrial dynamics: overview of molecular mechanisms.

36 Fry, M. Y. *et al.* In situ architecture of Opa1-dependent mitochondrial cristae remodeling.

37 Gilkerson, R., De La Torre, P. & St Vallier, S. Mitochondrial OMA1 and OPA1 as Gatekeepers of Organellar Structure/Function and Cellular Stress Response.

38 Anand, R. *et al.* The i-AAA protease YME1L and OMA1 cleave OPA1 to balance mitochondrial fusion and fission.

39 MacVicar, T. & Langer, T. A.-O. OPA1 processing in cell death and disease - the long and short of it.

40 Baker, M. J. *et al.* Stress-induced OMA1 activation and autocatalytic turnover regulate OPA1-dependent mitochondrial dynamics.

41 Zorova, L. D. *et al.* Mitochondrial membrane potential.

42 Rivera-Mejías, P. *et al.* The mitochondrial protease OMA1 acts as a metabolic safeguard upon nuclear DNA damage.

43 Adibi, R., Moein, S. & Gheisari, Y. Zoledronic acid targets chemo-resistant polyploid giant cancer cells. *Scientific Reports* **13**, 419 (2023). https://doi.org:10.1038/s41598-022-27090-1

44 Schieber, M. & Chandel, N. S. ROS function in redox signaling and oxidative stress.

45 Srinivas, U. S., Tan, B. W. Q., Vellayappan, B. A. & Jeyasekharan, A. D. ROS and the DNA damage response in cancer.

46 Malhotra, J. D. *et al.* Antioxidants reduce endoplasmic reticulum stress and improve protein secretion.

47 Wang, B. *et al.* ROS-induced lipid peroxidation modulates cell death outcome: mechanisms behind apoptosis, autophagy, and ferroptosis. *Archives of Toxicology* **97**, 1439-1451 (2023). https://doi.org:10.1007/s00204-023-03476-6

48 Iqbal, S. & Hood, D. A. Oxidative stress-induced mitochondrial fragmentation and movement in skeletal muscle myoblasts.

49 Ježek, J. A.-O. X., Cooper, K. F. & Strich, R. Reactive Oxygen Species and Mitochondrial Dynamics: The Yin and Yang of Mitochondrial Dysfunction and Cancer Progression. LID - 10.3390/antiox7010013 [doi] LID - 13.

50 Wu, S., Zhou F Fau - Zhang, Z., Zhang Z Fau - Xing, D. & Xing, D. Mitochondrial oxidative stress causes mitochondrial fragmentation via differential modulation of mitochondrial fission-fusion proteins.

51 Lee, H. C. & Wei, Y. H. Mitochondrial biogenesis and mitochondrial DNA maintenance of mammalian cells under oxidative stress.

52 Chang, X. *et al.* ROS-Drp1-mediated mitochondria fission contributes to hippocampal HT22 cell apoptosis induced by silver nanoparticles. *Redox Biology* **63**, 102739 (2023). https://doi.org:https://doi.org/10.1016/j.redox.2023.102739

53 Song, Q. *et al.* Evolutionary adaptation and asymmetric inheritance of polyploid giant cancer cells in esophageal squamous cell carcinoma. *Cancer Letters*, 217818 (2025). https://doi.org:https://doi.org/10.1016/j.canlet.2025.217818

54 Díaz, J. F., Valpuesta, J. M., Chacón, P., Diakun, G. & Andreu, J. M. Changes in Microtubule Protofilament Number Induced by Taxol Binding to an Easily Accessible

589 Site: INTERNAL MICROTUBULE DYNAMICS*. *Journal of Biological Chemistry* **273**, 33803-
590 33810 (1998). https://doi.org:https://doi.org/10.1074/jbc.273.50.33803
591 55 Dasari, S. & Tchounwou, P. B. Cisplatin in cancer therapy: molecular mechanisms of
592 action.
593 56 Lee, H. A.-O., Smith, S. B., Sheu, S. A.-O. & Yoon, Y. A.-O. The short variant of optic
594 atrophy 1 (OPA1) improves cell survival under oxidative stress.
595 57 Cogliati, S., Enriquez, J. A. & Scorrano, L. Mitochondrial Cristae: Where Beauty Meets
596 Functionality.
597 58 Decker, S. T. & Funai, K. Mitochondrial membrane lipids in the regulation of bioenergetic
598 flux.
599 59 Abrisch, R. G., Gumbin, S. C., Wisniewski, B. T., Lackner, L. L. & Voeltz, G. K. Fission and
600 fusion machineries converge at ER contact sites to regulate mitochondrial morphology.
601 LID - 10.1083/jcb.201911122 [doi] LID - e201911122.
602 60 Sonn, S. K. *et al.* ER-associated CTRP1 regulates mitochondrial fission via interaction with
603 DRP1. *Experimental & Molecular Medicine* **53**, 1769-1780 (2021).
604 https://doi.org:10.1038/s12276-021-00701-z
605 61 Chakrabarti, R. A.-O. *et al.* INF2-mediated actin polymerization at the ER stimulates
606 mitochondrial calcium uptake, inner membrane constriction, and division.
607 62 Ji, W.-k., Hatch, A. L., Merrill, R. A., Strack, S. & Higgs, H. N. Actin filaments target the
608 oligomeric maturation of the dynamin GTPase Drp1 to mitochondrial fission sites. *eLife*
609 **4**, e11553 (2015). https://doi.org:10.7554/eLife.11553
610 63 Gatti, P., Schiavon, C., Cicero, J., Manor, U. & Germain, M. Mitochondria- and ER-
611 associated actin are required for mitochondrial fusion. *Nature Communications* **16**, 451
612 (2025). https://doi.org:10.1038/s41467-024-55758-x
613 64 Moltedo, O., Remondelli, P. & Amodio, G. The Mitochondria-Endoplasmic Reticulum
614 Contacts and Their Critical Role in Aging and Age-Associated Diseases.
615 65 Fernández Casafuz, A. B., De Rossi, M. C. & Bruno, L. Mitochondrial cellular organization
616 and shape fluctuations are differentially modulated by cytoskeletal networks. *Scientific*
617 *Reports* **13**, 4065 (2023). https://doi.org:10.1038/s41598-023-31121-w
618 66 Choudhury, S. A.-O., Ananthanarayanan, V. A.-O. & Ayappa, K. A.-O. X. Coupling of
619 mitochondrial population evolution to microtubule dynamics in fission yeast cells: a
620 kinetic Monte Carlo study.
621 67 Daverey, A. *et al.* Depletion of mitochondrial protease OMA1 alters proliferative
622 properties and promotes metastatic growth of breast cancer cells. *Scientific Reports* **9**,
623 14746 (2019). https://doi.org:10.1038/s41598-019-49327-2
624 68 Chen, L. *et al.* Inhibition of mitochondrial OMA1 ameliorates osteosarcoma
625 tumorigenesis. *Cell Death & Disease* **15**, 786 (2024). https://doi.org:10.1038/s41419-
626 024-07127-1
627 69 Wu, Z. A.-O. *et al.* OMA1 reprograms metabolism under hypoxia to promote colorectal
628 cancer development.
629 70 Schneider, C. A., Rasband, W. S. & Eliceiri, K. W. NIH Image to ImageJ: 25 years of image
630 analysis. *Nature Methods* **9**, 671-675 (2012). https://doi.org:10.1038/nmeth.2089
631 71 Chaudhry, A., Shi, R. & Luciani, D. A.-O. A pipeline for multidimensional confocal analysis
632 of mitochondrial morphology, function, and dynamics in pancreatic β-cells.

72 RStudio: Integrated Development Environment for R (Posit Software, PBC, Boston, MA, 2025).
73 Valero-Mora, P. M. ggplot2: Elegant Graphics for Data Analysis. *Journal of Statistical Software, Book Reviews* **35**, 1 - 3 (2010). https://doi.org:10.18637/jss.v035.b01
74 Stirling, D. R. *et al.* CellProfiler 4: improvements in speed, utility and usability. *BMC Bioinformatics* **22**, 433 (2021). https://doi.org:10.1186/s12859-021-04344-9
75 Kostecka, L. A.-O. *et al.* Cancer cells employ lipid droplets to survive toxic stress.
76 Lefebvre, A., Ma, D., Kessenbrock, K., Lawson, D. A.-O. & Digman, M. A.-O. Automated segmentation and tracking of mitochondria in live-cell time-lapse images.

ACKNOWLEDGEMENTS
This work was also supported by the William and Carolyn Stutt Research Fund, Ronald Rose, MC Dean, Inc., William and Marjorie Springer, Mary and Dave Stevens, Louis Dorfman, and the Jones Family Foundation. We thank the Johns Hopkins School of Medicine Microscope Facility for the acquisition of transmission electron microscopy images with the ThermoFisher Talos L120C.

FUNDING
This work was supported by the US Department of Defense CDMRP/PCRP 367 (W81XWH-20-10353), the Prostate Cancer Foundation, and the Patrick C. Walsh Prostate Cancer Research Fund to SRA; and NCI grants U54CA143803, CA163124, CA093900, and CA143055, and the Prostate Cancer Foundation to KJP. This work was also supported by the Office of the Director and the National Institute of General Medical Sciences of the National Institutes of Health under award number S10OD023548.

AUTHOR CONTRIBUTIONS
Conceptualization: ML, KJP, SRA; Experimental work: ML, CAM, LTAR, QN, ZG; Data analysis and figure generation: ML; Writing – original draft preparation: ML; Writing – review and editing: ML, KJP, SRA. Funding acquisition: SXS, KJP, SRA.

COMPETING INTERESTS
KJP is a consultant to Cue Biopharma, Inc., an equity holder in PEEL Therapeutics, and a founder and equity holder in Keystone Biopharma, Inc. SRA is an equity holder in Keystone Biopharma, Inc.

ETHICS DECLARATIONS
Approval for animal experiments: Not applicable

Approval for human experiments: Not applicable

Consent to participate/consent to publish: Not applicable

SUPPLEMENTARY INFORMATION
Supplementary Figure S1. N-acetyl cysteine decreases levels of reactive oxygen species in cells 10 Days Post-Treatment Removal. **(a)** Representative DCF-DA fluorescence images of cells treated with N-acetyl cysteine and vehicle. (**b**) Quantification of mean fluorescence intensity of DCF-DA between indicated groups.
Supplementary Figure S2. Uncropped blot images from Figure 2a. Boxed areas delineate the cropped portion displayed in Figure 2a.

682 **Supplementary Figure S3**. Uncropped blot images from Figure 3a. Boxed areas delineate the
683 cropped portion displayed in Figure 3a.
684 **Supplementary Video 1.** Representative time lapse of mitochondrial dynamics in untreated
685 PC3 cells stained with MitoTracker Green.
686 **Supplementary Video 2.** Second representative time lapse of mitochondrial dynamics in
687 untreated PC3 cells stained with MitoTracker Green.
688 **Supplementary Video 3.** Representative time lapse of mitochondrial dynamics in cells 10 Days
689 Post-Treatment Removal stained with MitoTracker Green.
690 **Supplementary Video 4.** Second representative time lapse of mitochondrial dynamics in cells
691 10 Days Post-Treatment Removal stained with MitoTracker Green.
692
693 **FIGURE LEGENDS**
694 **Figure 1. Cancer cells surviving chemotherapy have increased levels of reactive oxygen**
695 **species and exhibit mitochondrial fragmentation**. (**a**) Timeline for the induction of the
696 chemotherapy-resistant cancer cell state. Created in BioRender. Li, M. (2025)
697 https://BioRender.com/vkhgx05 (**b**) Phase contrast images of untreated cells and cells 1- and
698 10-Days Post-Treatment Removal (PTR). (**c**) Cell volume measurements of untreated cells and
699 cells 1- and 10-Days PTR. (**d**) Phase contrast images and DCF-DA fluorescence images in
700 untreated cells and cells 10 Days PTR. (**e**) Quantification of mean fluorescence intensity of
701 DCF-DA staining. (**f**) Representative images of TOM20 and Phalloidin in untreated cells and
702 cells 10 Days PTR. Segmentation of TOM20 signal was performed to quantify mitochondrial
703 morphology features. (**g**) Quantification of number of mitochondria per cell. (**h**) Quantification of
704 mitochondria normalized to cell area. (**i**) Quantification of number of branches per
705 mitochondrion. (**j**) Quantification of branch length per mitochondrion. n = 679, 257, and 249 cells
706 for untreated, cells 1 Day PTR, and cells 10 Days PTR, respectively (**c**); n = 1141 and 362 cells
707 for untreated and cells 10 Days PTR, respectively (**e**); n = 37 and 22 cells for untreated and
708 cells 10 Days PTR, respectively (**g-j**). Data are presented as mean ± s.e.m. (**c**, **g-j**), while data
709 in violin plots were presented as median and corresponding interquartile ranges (**e**). p values
710 were calculated with a one-way ANOVA followed by a post-hoc Tukey's multiple comparisons
711 test (**c**), a two-tailed Mann Whitney test (**e**), and an unpaired Student's two-tailed t-test (**g-j**). ns
712 not significant, **** $p<0.0001$.
713
714 **Figure 2. Cells 10 Days PTR increase DRP1 localization to mitochondria**. (**a**)
715 Representative western blots of Phospho-DRP1 Ser637, Phospho-DRP1 Ser616, DRP1, MFF,
716 MiD49, MiD51, and β-actin loading control. n = 3 biological replicates. We note that due to
717 similarities in molecular weight and identical primary antibody species, each protein was probed
718 independently on separate blots with their own separate β-actin loading control. Original,
719 uncropped blots (including the β-actin loading control for each blot) are presented in
720 Supplementary Figure S2. (**b**) Max intensity projection images of TOM20 and DRP1 channels in
721 untreated cells and cells 10 Days PTR. (**c**) Normalized profile intensity plot of TOM20 and DRP1
722 signal in untreated cells. (**d**) Normalized profile intensity plot of TOM20 and DRP1 signal in cells
723 10 Days PTR. (**e**) 3-dimensional (3D) rendering of TOM20, DRP1, and Phalloidin signal in
724 untreated cells and cells 10 Days PTR. (**f**) Quantification of TOM20-DRP1 colocalization in 3D.
725 n = 11 cells each for untreated and cells 10 Days PTR (**f**). Data are presented as mean ± s.e.m.
726 in (**f**), and p values were calculated with an unpaired Student's two-tailed t-test (**f**). ** $p<0.01$.
727
728 **Figure 3. Mitochondria in cells 10 Days PTR have aberrant cristae morphology**. (**a**)
729 Representative western blots of OPA1, OMA1, Vinculin, and β-actin loading control. We note
730 that due to similarities in molecular weight and identical primary antibody species, each protein
731 was probed independently on separate blots with their own separate β-actin or vinculin loading
732 control. Original, uncropped blots (including the β-actin or vinculin loading control for each blot)

are presented in Supplementary Figure S3. **b**) Quantifications of OPA1 isoform protein expression in untreated cells and cells 10 Days PTR. Samples derive from the same experiment in each blot that was quantified. (**c**) Quantification of OMA1 expression in untreated cells and cells 10 Days PTR. Samples derive from the same experiment in each blot that was quantified. (**d**) Representative transmission electron microscopy (TEM) images of mitochondria in untreated cells and cells 10 Days PTR. (**e**) Quantification of number of cristae per mitochondrion. (**f**) Quantification of mean cristae area per mitochondrion. (**g**) Quantification of cristae width. (**h**) Quantification of mitochondrial area between untreated cells and cells 10 Days PTR. (**i**) Representative fluorescence images of MitoTracker Red CMXRos staining in untreated cells and cells 10 Days PTR. (**j**) Quantification of mean fluorescence intensity of MitoTracker Red CMXRos staining between indicated groups. n = 4 biological replicates (**b**); n = 3 biological replicates (**c**); n = 42 and 59 mitochondria for untreated and cells 10 Days PTR, respectively (**e-f, h**); n = 229 and 177 cristae for untreated and cells 10 Days PTR, respectively (**g**); n = 12,147 and 2502 cells for untreated and cells 10 Days PTR, respectively (**j**). Data are presented as mean ± s.e.m. (**b-c**), while data in violin plots are presented as median and corresponding interquartile ranges (**e-h, j**). p values were calculated with a two-tailed Kolmogorov-Smirnov test (**e-h**), and a two-tailed Mann-Whitney test (**j**). * $p<0.05$, ** $p<0.01$, **** $p<0.0001$.

Figure 4. Cells 10 Days PTR decrease both mitochondrial fission and fusion dynamics. (**a**) Representative fluorescence images of mitochondria every 60 seconds for 6 minutes in untreated cells and cells 10 Days PTR. Yellow arrow and box indicate a fusion event, while a blue arrow and box indicate a fission event. (**b**) Linear regression analysis of fission rate vs mitochondrial area. (**c**) Linear regression analysis of fusion rate vs mitochondrial area. (**d**) Quantification of fission rate in untreated cells and cells 10 Days PTR when normalized to mitochondrial area. (**e**) Quantification of fusion rate in untreated cells and cells 10 Days PTR when normalized to mitochondrial area. n = 37 and 17 cells for untreated and cells 10 Days PTR, respectively (**b-c, d-e**). Data are presented as scatter plots (**b-c**) and mean ± s.e.m. (**d-e**). R-squared values were calculated with the lm() and summary() functions in RStudio[72] (**b-c**). p values were calculated with the lm() and summary() functions in RStudio[72] (**b-c**) and a two-tailed Mann-Whitney test (**d-e**). * $p<0.05$, ** $p<0.01$.

Figure 5. Cancer cells surviving chemotherapy increase OMA1 activity and decrease mitochondrial fusion and function to combat oxidative stress. Cancer cells that survive chemotherapy enter a resistant cell state that increases their cell size and remain non-proliferative. Cells in this state have increased levels of reactive oxygen species (ROS) and exhibit fragmented mitochondria. Cells in this state increase OMA1 activity, cleaving L-OPA1 to S-OPA1, ultimately disrupting the mitochondrial cristae structure and reducing mitochondrial fusion. This altered cristae structure generates a diffuse proton gradient and decreases mitochondrial membrane potential, which lowers oxidative capacity and endogenous ROS production as a survival mechanism against oxidative stress in these cells. Created in BioRender. Li, M. (2025) https://BioRender.com/41jh49x.

Fig. 1

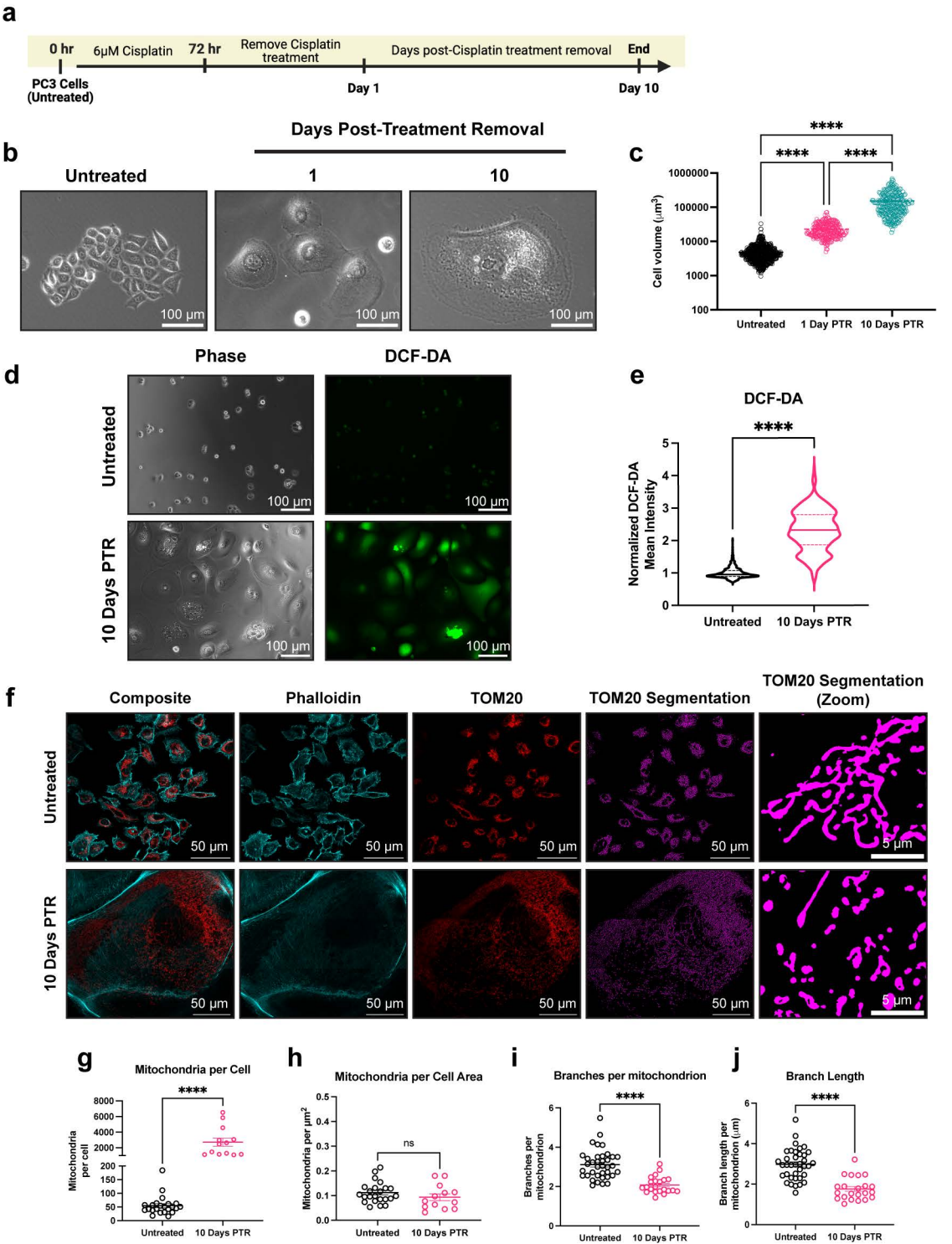
a
0 hr
6μM Cisplatin
72 hr
Remove Cisplatin treatment
Days post-Cisplatin treatment removal
End
PC3 Cells (Untreated)
Day 1
Day 10
b
Days Post-Treatment Removal
Untreated
1
10
100 μm
c
****
Cell volume (μm³)
1000000
100000
10000
1000
100
Untreated
1 Day PTR
10 Days PTR
d
Phase
DCF-DA
Untreated
10 Days PTR
100 μm
e
DCF-DA
Normalized DCF-DA Mean Intensity
Untreated
10 Days PTR
f
Composite
Phalloidin
TOM20
TOM20 Segmentation
TOM20 Segmentation (Zoom)
Untreated
10 Days PTR
50 μm
5 μm
g
Mitochondria per Cell
Mitochondria per cell
h
Mitochondria per Cell Area
Mitochondria per μm²
ns
i
Branches per mitochondrion
Branches per mitochondrion
j
Branch Length
Branch length per mitochondrion (μm)

Fig. 2

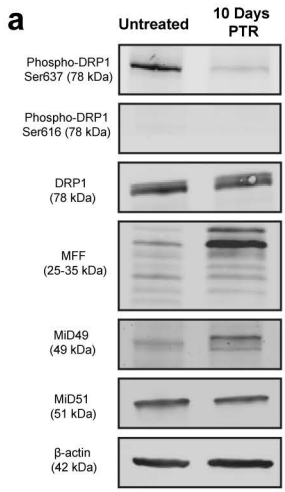
a
Untreated
10 Days PTR
Phospho-DRP1 Ser637 (78 kDa)
Phospho-DRP1 Ser616 (78 kDa)
DRP1 (78 kDa)
MFF (25-35 kDa)
MiD49 (49 kDa)
MiD51 (51 kDa)
β-actin (42 kDa)

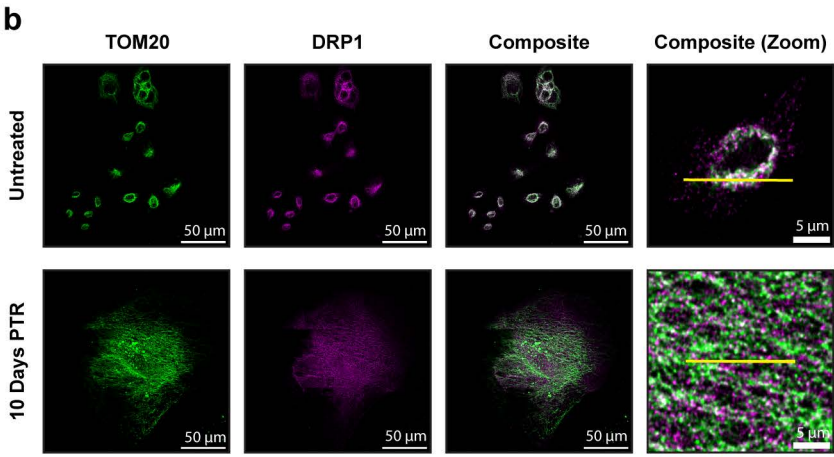
b
TOM20
DRP1
Composite
Composite (Zoom)
Untreated
10 Days PTR
50 µm
5 µm

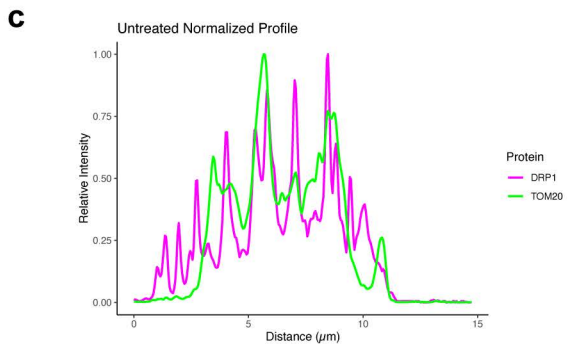
c
Untreated Normalized Profile
Relative Intensity
Distance (µm)
Protein
DRP1
TOM20

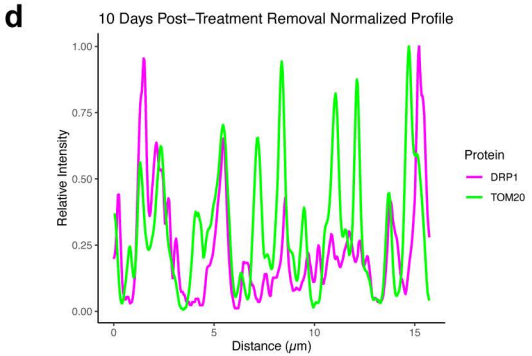
d
10 Days Post–Treatment Removal Normalized Profile
Relative Intensity
Distance (µm)
Protein
DRP1
TOM20

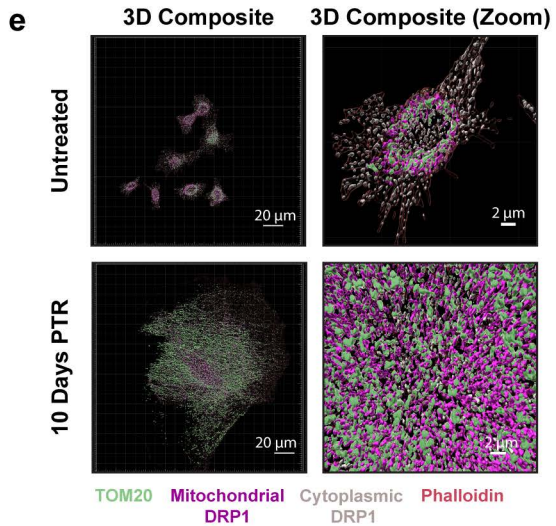
e
3D Composite
3D Composite (Zoom)
Untreated
10 Days PTR
20 µm
2 µm
TOM20
Mitochondrial DRP1
Cytoplasmic DRP1
Phalloidin

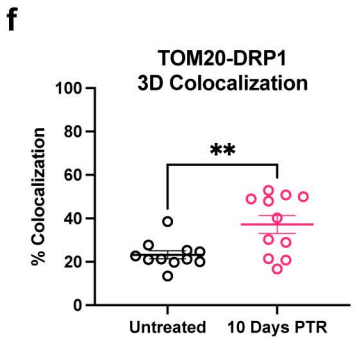
f
TOM20-DRP1
3D Colocalization
% Colocalization
**
Untreated
10 Days PTR

Fig. 3

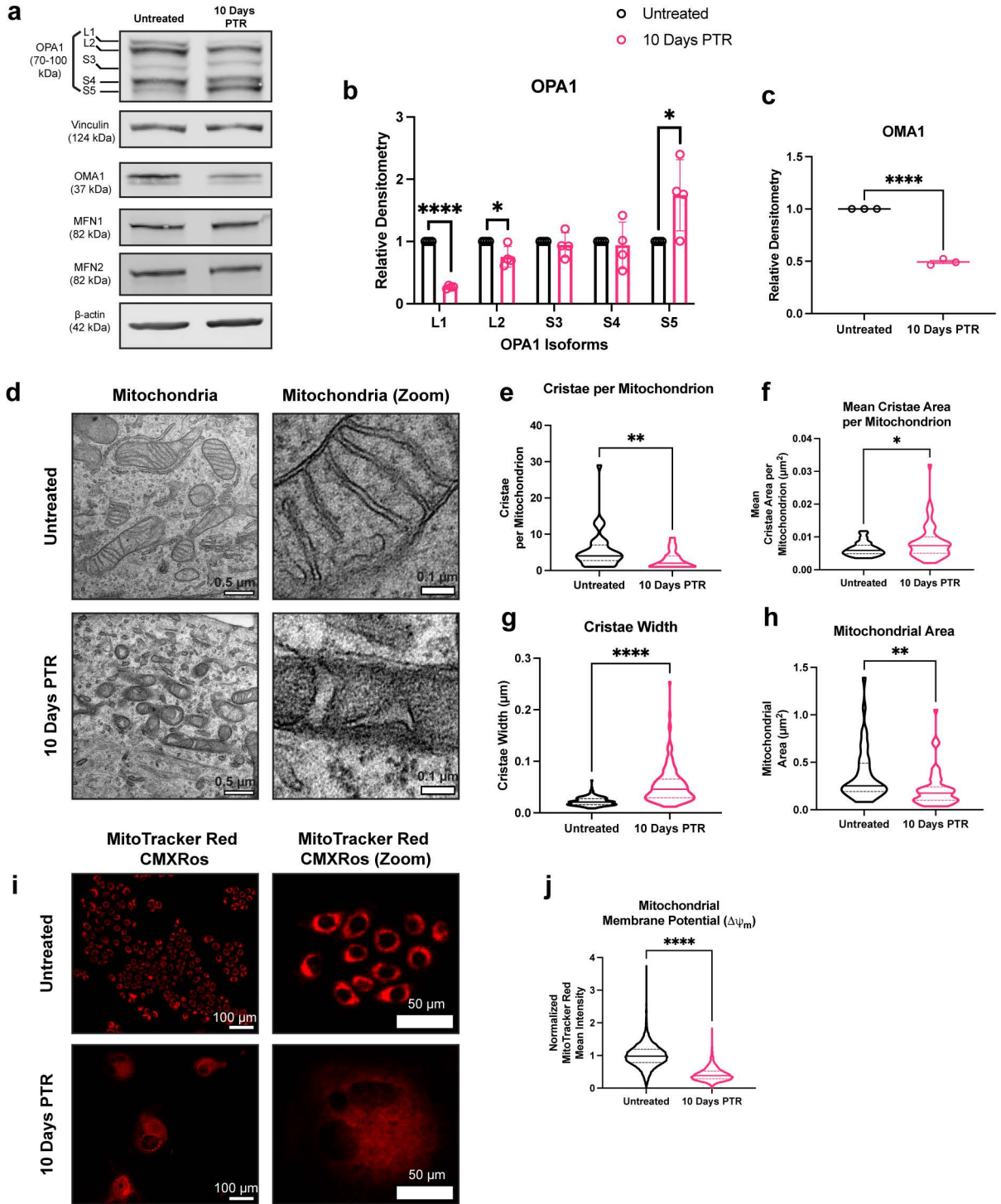
a
Untreated
10 Days PTR
OPA1 (70-100 kDa)
L1
L2
S3
S4
S5
Vinculin (124 kDa)
OMA1 (37 kDa)
MFN1 (82 kDa)
MFN2 (82 kDa)
β-actin (42 kDa)
Untreated
10 Days PTR
b
OPA1
Relative Densitometry
OPA1 Isoforms
L1
L2
S3
S4
S5
****
*
*
c
OMA1
Relative Densitometry
****
Untreated
10 Days PTR
d
Mitochondria
Mitochondria (Zoom)
Untreated
10 Days PTR
0.5 µm
0.1 µm
e
Cristae per Mitochondrion
Cristae per Mitochondrion
**
f
Mean Cristae Area per Mitochondrion
Mean Cristae Area per Mitochondrion (µm²)
*
g
Cristae Width
Cristae Width (µm)
****
h
Mitochondrial Area
Mitochondrial Area (µm²)
**
i
MitoTracker Red CMXRos
MitoTracker Red CMXRos (Zoom)
Untreated
10 Days PTR
100 µm
50 µm
j
Mitochondrial Membrane Potential (Δψm)
Normalized MitoTracker Red Mean Intensity
****

Fig. 4

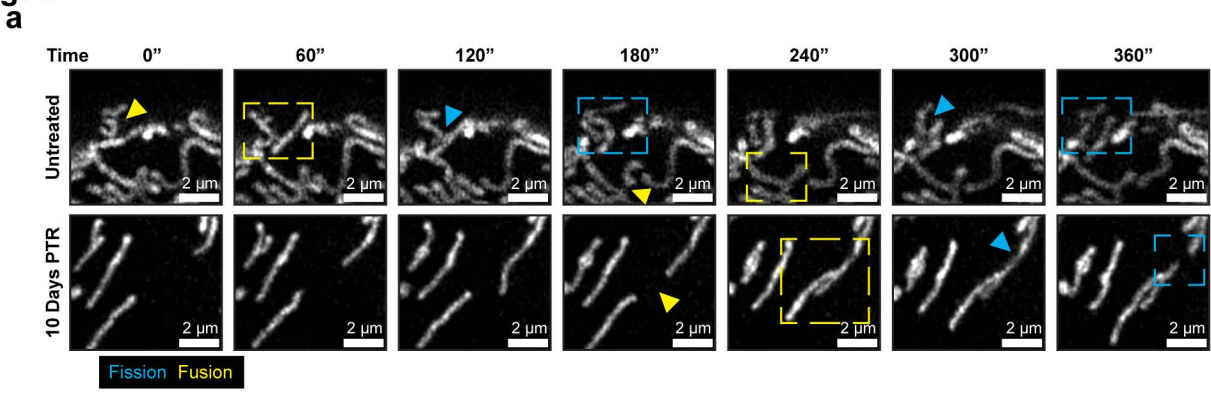
a
Time
0”
60”
120”
180”
240”
300”
360”
Untreated
10 Days PTR
2 µm
Fission
Fusion

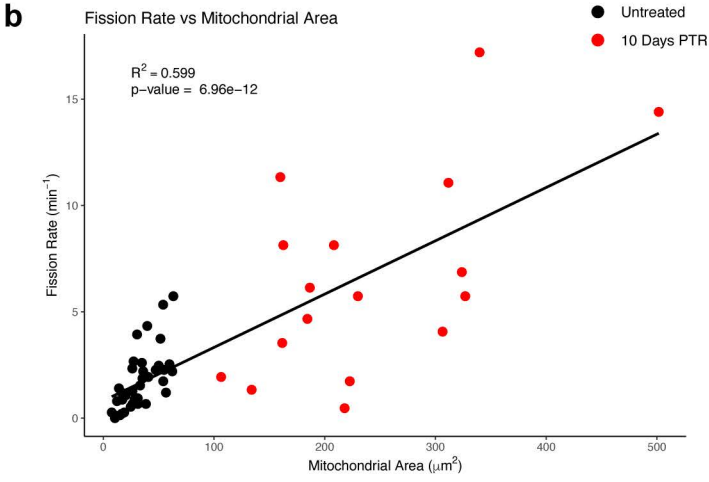
b
Fission Rate vs Mitochondrial Area
Untreated
10 Days PTR
$R^2 = 0.599$
p–value = 6.96e–12
Fission Rate (min^{-1})
Mitochondrial Area (µm^2)
0
5
10
15
0
100
200
300
400
500

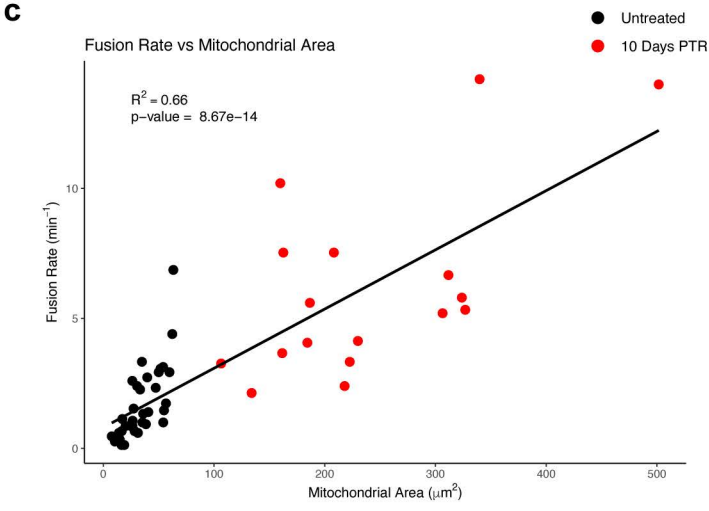
c
Fusion Rate vs Mitochondrial Area
Untreated
10 Days PTR
$R^2 = 0.66$
p–value = 8.67e–14
Fusion Rate (min^{-1})
Mitochondrial Area (µm^2)
0
5
10
0
100
200
300
400
500

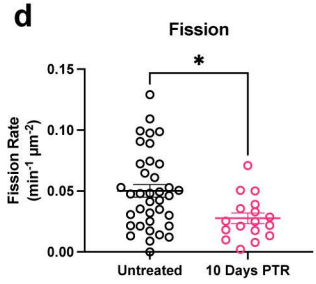
d
Fission
*
Fission Rate (min^{-1} µm^{-2})
0.00
0.05
0.10
0.15
Untreated
10 Days PTR

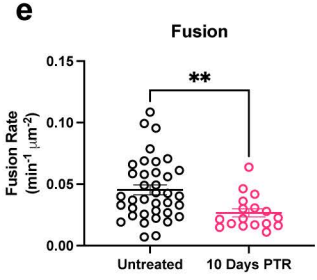
e
Fusion
**
Fusion Rate (min^{-1} µm^{-2})
0.00
0.05
0.10
0.15
Untreated
10 Days PTR

Fig. 5

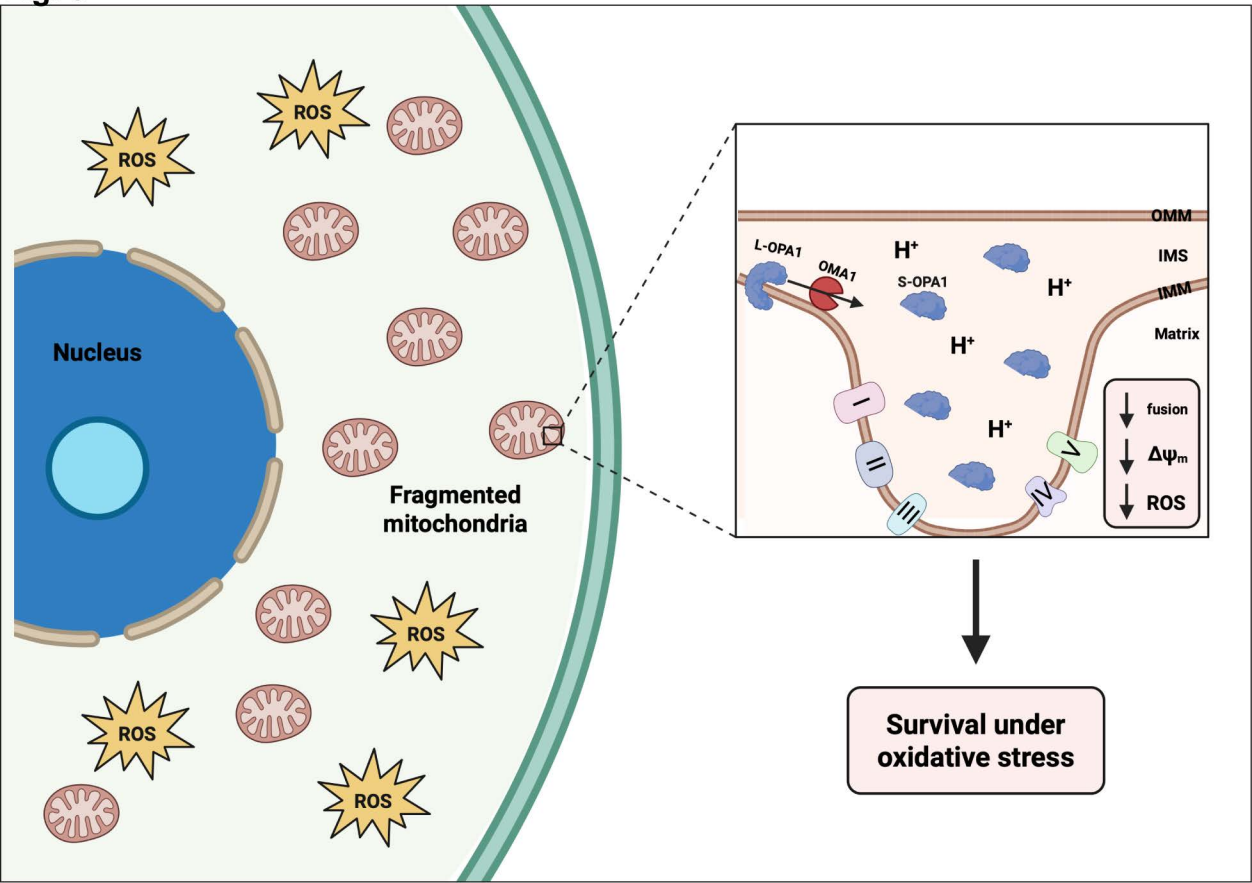
ROS
ROS
Nucleus
Fragmented mitochondria
ROS
ROS
ROS
OMM
IMS
IMM
Matrix
L-OPA1
OMA1
S-OPA1
H+
H+
H+
H+
I
II
III
IV
V
fusion
Δψm
ROS
Survival under oxidative stress